Supplementary Information

An ultra-sensitive hydrogen gas sensor using reduced graphene oxide-loaded ZnO nanofibers

Zain Ul Abideen,[a] Hyoun Woo Kim,*[b] Sang Sub Kim,*[a]

[a] *Department of Materials Science and Engineering, Inha University, 100 Inha-ro, Nam-gu, Incheon 402-751, Republic of Korea E-mail: sangsub@inha.ac.kr; Fax: +82-32-862-5546; Tel: +82-32-860-7546*

[b] *Division of Materials Science and Engineering, Hanyang University, 222 Wangsimni-ro, Seongdong-Gu, Seoul, 133-791, Republic of Korea. E-mail: hyounwoo@hanyang.ac.kr; Tel: +82-2220-0382*

Text S1. Experimental Methods

Materials

Zinc acetate ($(CH_3CO_2)_2Zn$), reduced graphene oxide (rGO), polyvinyl alcohol (MW 80,000), tin(II) chloride dihydrate, polyvinylpyrrolidone (MW 13,00,000), ethanol (anhydrous, 99.5%), and dimethylformamide (DMF, anhydrous, 99.8%) were obtained from Sigma Aldrich Corp. and were used as received without any further processing or refining.

Preparation of rGO nanosheets

Graphite powder, H_2SO_4 (98%), H_3PO_4 (98%), $KMnO_4$ (98%) and H_2O_2 (30 wt%), Hydrazine monohydrate (98%), N,N-Dimethylformamide (DMF, 99.8%) were obtained from commercial resources and used as received. GO was synthesized from graphite powder via a modification of Hummers and Offeman's method from graphite powders.[1] In a typical reaction, 5g of graphite, 60 mL of H_3PO_4, and 180 mL of H_2SO_4 were stirred together with a Teflon-coated magnetic stirring in an ice bath. Next, 60 g of $KMnO_4$ was slowly added while the temperature was maintained at $0\,^{\circ}C$. Once mixed, the solution is transferred to a $35 \pm 5\,^{\circ}C$ water bath and stirred for 3 h, forming a thick paste. Next, distilled water (450 mL) was slowly dropped into the resulting paste to dilute the mixture, and then the solution was stirred for 1 h while the temperature was raised to $90 \pm 5\,^{\circ}C$. Finally, 800 mL of distilled water was added, followed by the slow

addition of 60 mL H_2O_2 (30%), turning the color of the solution from dark brown to yellow. During this final step, H_2O_2 (30%) reduced the residual permanganate and manganese dioxide to colorless soluble manganese sulfate. The GO deposit was collected from the GO suspension by high speed centrifugation at 15000 rpm for 30 min. The obtained GO was then washed with 1000 mL of HCl (5%), and repeatedly washed with distilled water until the pH = 7. To obtain uniform GO, a low-speed centrifugation at 3000 rpm was first used to remove thick multilayer sheets until all the visible particles were removed (3-5 min). Then the supernatant was further centrifuged at 10000 rpm for 30 min to remove small GO pieces and water-soluble byproduct. The final sediment was redispersed in 500 ml of DMF with mild sonication, resulting in a solution of exfoliated GO. In general, for chemically reduced GO (rGO), 500 ml of exfoliated GO was stirred for 30 min, and 10 ml of hydrazine monohydrate was added. The mixtures were heated at 150 ± 5 ^{o}C using an oil bath for 24 h; a black solid precipitated from the reaction mixtures. Products were collected by centrifugation at 12000 rpm for 45 min and washed with DI water and methanol until the pH = 7. Next, the obtained rGO was dried and stored in a vacuum oven at 60°C until use .

Synthesis of rGO-loaded ZnO and rGO-loaded SnO$_2$ composite NFs

The preparation of the precursor solution used to fabricate rGO-loaded ZnO composite NFs was prepared by dissolving 10 wt% polyvinyl alcohol in distilled water, and the mixture was constantly stirred for 4h at 70ºC. Then, 1 g of zinc acetate and a 0.44 wt% rGO solution were added to the mixture and continuously stirred for 6h at 70ºC. The precursor solution used to synthesize rGO-loaded SnO$_2$ was prepared by mixing 8 wt% polyvinylpyrrolidone into a 1:1 solvent mixture of DMF and ethanol under constant stirring for 4h at room temperature. Then, 1.75 g of SnCl$_2$.2H$_2$O and a 0.44 wt% rGO solution were added to the mixture and constantly stirred for 12h at room temperature. The amount of rGO loaded in both SnO$_2$ and ZnO NFs was maintained at 0.44 wt%, which was previously determined to be optimal.[2]

The prepared Zn and Sn precursor solutions were used for electrospinning by loading into syringes with needles of an inner diameter of 0.51 mm. The distance between the tip of the needle and the collector was fixed at 20 cm. The feed rates of the solutions were set to 0.05 ml/h using an accurate syringe pump. As-spun NFs collected over a Si wafer with a 250-nm-thick SiO$_2$ layer were subsequently heated at 600ºC in air for 30 min at a heating rate of 0.5ºC/min to remove the polymer solvents. All experiments were performed at room temperature. Details of the processes used to synthesize the electrospun NFs can be found in our earlier reports.[3,4]

Characterization and sensing measurements

The morphology and microstructure of the synthesized NFs were examined using field-emission scanning electron microscopy (FE-SEM, Hitachi S-4200) and transmission electron microscopy (TEM, Philips CM-200), respectively. Raman and XPS analyses were performed to reveal the incorporation of the rGO nanosheets. The Raman spectra were acquired using a Jasco laser Raman spectrophotometer *NRS-3000* series, with an excitation laser wavelength of 532 nm at a power density of 2.9 mW·cm^{-2}. Micro-Raman spectra were obtained using a Raman microscope (LabRam HR800 UV; Horiba Jobin-Yvon, France) at the Korea Basic Science Institute (KBSI), scanning from 85 to 3000 cm^{-1} at room temperature in open air. A diode laser with a wavelength of 514 nm was used for Raman excitation. The Raman spectrum of rGO-loaded ZnO NFs is presented in the Supporting Information (Fig. S1). The A1(TO), E$_2$(high), and A$_1$(LO)/E1(LO) peaks of ZnO were observed at 365, 445, and 559 cm^{-1}, respectively.[5] The D and G bands of rGO were observed at 1384 and 1601 cm^{-1}, respectively. XPS was performed using a VG Multilab ESCA 2000 system, in which a monochromatized AlKα X-ray source (hν = 1486.6 eV) was used.

In order to evaluate the sensing properties of the synthesized NFs, Ti (thickness: ~50 nm) and Pt (thickness: ~200 nm) were sequentially deposited on the substrates via magnetron sputtering using interdigital electrodes. A custom-made gas dilution and sensing system was used to measure the sensor responses to a range of concentrations of hydrogen gas (0.1 – 10 ppm) at 300, 350, 400 and 450ºC. A known amount of

5

high-purity hydrogen gas (>99.999%) was transferred from the storage cylinder to the sensing chamber, and the desired concentration was obtained by diluting with N_2 gas and controlling the conductance change of the sensors in the absence and presence of hydrogen, where R_a is the resistance in the absence and R_g is the resistance in the presence of hydrogen. The response and recovery times were calculated by measuring the times needed to reach a 90% change in the resistance on the supply or removal of hydrogen.

Text S2.

We investigated the microstructure and morphology of rGO-loaded SnO_2 NFs by using FE-SEM and TEM (Fig. S2). The calcination did not significantly change the morphology of the NFs (Fig. S2a and S2b). By means of calcination at 600ºC for 0.5 h in air at a heating rate of 0.5ºC/min, the NFs exhibited a large number of nanograins with an average size of 35 nm (Fig S2b). It is noteworthy that the grains in NFs were uniform in size and shape. The inset figures of Figs. S2a and S2b show the low-resolution SEM micrograph, revealing the relatively uniform distribution of the straight-line NFs on the Si/SiO_2 substrates. Fig. S2c, which corresponds to a low-magnification TEM image, confirms the polycrystalline nature of the rGO-loaded SnO_2 NFs with the presence of nanograins, agreeing with SEM micrographs (Fig. S2b). Fig. S2d shows the lattice-resolved TEM image of the surface region of the rGO-loaded SnO_2 NF in Fig. S2c. Besides the crystalline SnO_2 structure, amorphous rGO nanosheet was observed on the surfaces of the nanograins, generating local heterojunctions with n-SnO_2 nanograins. The inter-planar distance of the NF was approximately 0.26 nm, corresponding to the (101) plane of the tetragonal SnO_2 phase (Fig. S2d). The diffraction ring patterns were indexed to (110), (101), (200), and (211) planes of a tetragonal SnO_2 structure (JCPDS Card No. 41-1445) (Fig. S2e). Figs. S2f and S2g exhibit the EDX spectra taken from the (f) and (g) positions in Fig. S2d, respectively. It is revealed that the position (f), which

7

has the rGO NSs on the surface, exhibits the much higher atomic ratio of C/Sn, than the position (g).

Text S3.

Alternatively, it is expected that the metallization of ZnO will be dependent on the sensing temperature, with hydrogen atoms inducing metallization of ZnO even at room temperature.[6,7] First, the diffusion coefficient of interstitial hydrogen D_H in ZnO is known to increase drastically by increasing the temperature from RT to 800 K.[8,9] Accordingly, the amount of H-loading on the ZnO surface will increase by increasing the sensing temperature.[8,9] Second, the associated metallization reactions are thermodynamically favorable at higher temperatures.

$$ZnO(s) + H_2(g) \rightarrow Zn(s) + H_2O(g) \qquad\qquad (1)$$
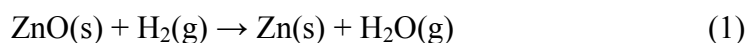
With adopting the standard free energy as $\Delta G° = 130{,}415 - 119.353T$ (kJ/mol),[10] those at 300, 350, and 400 ℃ are calculated to be about 62.01, 56.04, and 50.07 kJ/mol, respectively.

In addition, it is possible that hydrogen adsorbed on Zn-polar surface is so reactive that it is able to reducing ZnO to metallic Zn, forming and desorbing OH groups by the following equation:[11]

ZnO(s) + H(g) → OH(g) + Zn(s)   (2)
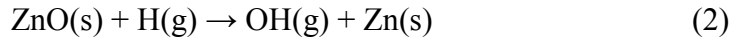
With adopting the standard free energy as $\Delta G° = 171{,}448\text{-}66.984\text{T}$ (kJ/mol),[10] those at 300, 350, and 400 °C are calculated to be about 133.06, 129.71, and 126.36 kJ/mol, respectively. Although the present sensing is not in its standard condition, the Zn metallization will be thermodynamically favorable at higher temperature.

Figure 3 in the manuscript text reveals that an increase in temperature from 300 to 400 °C increased the sensor response of rGO-laoded ZnO NFs by approximately 150%, whereas that of rGO-laoded SnO_2 NFs was increased by approximately 87.5%. Accordingly, the additional increase in the sensor response of rGO-loaded ZnO NFs with increasing temperature is associated with the observation that ZnO metallization is enhanced at high temperature.

Text S4.

It has been revealed that the maximum sensing temperature of metal oxides such as SnO_2 and ZnO can be varied over large temperature range, depending on many factors, which are not yet clearly known. There are several factors which affect the hydrogen sensing behavior. First, the redox reaction, in which the hydrogen molecules will react with the adsorbed oxygen species, is exothermic and will be activated or enhanced at higher temperature. Second, the adsorption and desorption of hydrogen will be important. At higher temperature, the adsorption of hydrogen will be suppressed and may be desorbed prior to the redox reaction, contributing to the depression of hydrogen sensing at higher temperature. Third, in case of ZnO sensor, hydrogen-induced metallization will affect the sensing behavior. The Zn metallization will be thermodynamically favorable at higher temperature. Accordingly, with the adsorption being suppressed at higher temperature, it is expected that the temperature-dependent sensing exhibits the bell-shaped behavior.

Text S5.

In Fig. 4 of the manuscript, it is depicted that a large amount of rGO NSs is discretely distributed in the ZnO NFs, without a direct contact between adjacent rGO NSs. With the assumption that there is no H_2 gas, since the work functions of n-ZnO and rGO were about 5.20 and 4.75 eV, respectively (Fig. 4 in the manuscript), the electrons will flow from metallic rGO to n-ZnO, ultimately equating the Fermi level of two components. Accordingly, at equilibrium, the potential barrier (~0.45 eV) will be formed when the rGO contacts the n-ZnO. It has been widely accepted that the presence of hydrogen on a ZnO surface noticeably enhances its electrical conductivity.[12,13] Surface hydrogen atoms are very shallow donors, forming strong bonds with surface O ions rather than incorporating into bulk ZnO.[14] These characteristics contribute to the surface metallization of ZnO. Among the several mechanisms regarding hydrogen-induced metallization[15-19], the ″reduction″ mechanism, also referred to as ″semiconductor to metallic transition″ or ″surface metallization effect,″ has been regarded as the most likely and explains the high sensitivity and selectivity to hydrogen in the case of pure ZnO NFs at high temperatures.[21] Hydrogen-induced metallicity has been observed on a variety of surfaces, including ZnO (100),[13,18,20] ZnO (0001),[15] and ZnO (2$\bar{1}\bar{1}$0).[17] The delocalization of charge between Zn and O-H bonds induces metallization of surface Zn atoms.[21] The surface state of ZnO before and after H_2 exposure was investigated using XPS in our previous work,[21] confirming the transformation of the ZnO surface to metallic Zn. Since the introduction of H_2 gas inevitably generates metallic Zn layer along the rGO/ZnO heterojunctions, the energy band diagrams involving three phases should be considered (Fig. 4 in the manuscript). With the work functions of rGO, Zn, and ZnO being 4.75, 4.33, and 5.20 eV, respectively, at equilibrium, the potential barriers not only at the rGO/Zn interfaces but also at the Zn/ZnO interfaces will be generated.

One possibility is that the n-ZnO will become more n-type, by the transfer of electrons from rGO. The above speculation is based on the assumption that the Zn metallic layer will not be generated. However, in reality, the metallic Zn layer will be provided upon the introduction of H_2 gas. In this case, n-ZnO will become much more n-type, by the transfer of electrons from metallic Zn. In this case, the adsorbed oxygen from ambient atmosphere will more efficiently extract electrons from ZnO, enlarging the depletion region and thus decreasing the conduction region.[22,23] The hydrogen molecules will react with the adsorbed oxygen species. The released electrons will reduce the thickness of the depletion region, and decrease the resistance of the semiconductors. Upon introduction and removal of H_2 gas, the conduction region will be increased and decreased, respectively (i.e. depletion region will be decreased and increased, respectively). Since the original volume of the conduction layer in ZnO NFs is larger by the ZnO/rGO heterointerfaces, the relative change of the resistance by the H_2 gas will be larger, resulting in the higher sensitivity. The second possibility is associated with the electron flow of ZnO through the rGO NSs, ultimately providing additional modulation of resistance. With the neighboring NSs being disconnected, the electrical conduction will mainly occur through the ZnO NFs. In air ambient, the equilibrium energy band of ZnO is 0.45 eV higher than that of rGO, facilitating easy flow of electrons from ZnO to rGO. For the realization of electrical conduction through the rGO NSs, the electrons, which were penetrated from the ZnO into the rGO, should be taken out of the rGO NSs. In air ambient, however, the reverse flow from rGO to n-ZnO is not efficient and electrons in rGO cannot easily escape out to the neighboring ZnO grains, owing to the barrier height (i.e. 0.45 eV). On the other hand, in H_2 ambient, the potential barrier of rGO/Zn will be established, preventing the electron flow into rGO. Accordingly, the electrons in sensor devices will be less lost to the rGO region. This will add to decrease of resistance by H_2 gas. As a third possibility, the rGO NSs will exert the spillover effect. The discretely distributed rGO NSs being attached to the surfaces of the NFs are nanostructures with a higher surface accessibility.[24] The NSs will exert a catalytic function in the adsorption, dissociation and migration of H_2 gas molecules. It is possible that the defects and functional groups on the rGO surface provide adsorption sites for the gas molecules and will increase the sensitivity.[22]

Text S6.

1) **Sensing mechanisms of rGO-loaded SnO$_2$ NFs**

In normal air ambient, the SnO$_2$ NFs have an electron-depletion layer underneath the surface, because adsorbed oxygen species extract electrons from the conduction band of *n*-type SnO$_2$. The electron-depletion layer will be reduced by the introduction of H$_2$ gas. There is a resistance modulation due to the change of the radial thickness of the electron-depletion layer. In addition, although it is possible that neighbouring individual NFs in their networked configuration will physically contact, providing further resistance modulation, it is reasonable to assume that the contribution of this type of resistance is negligible in comparison to other sources of resistance. Second, there is a resistance modulation due to the change of the height of the potential barrier at nanograin boundaries, usually operating in polycrystalline sensor materials. In the case of *n*-type semiconductors, oxygen species in air diffuse along the grain boundaries and build up upward band bending, becoming a barrier to electron transport. The potential barrier increases by introduction of oxidizing gas molecules in air ambient. The potential barrier will decrease by outdiffusion of pre-adsorbed oxygen species under a H$_2$ gas environment. In addition, the sensing mechanism associated with rGO NS-loaded SnO$_2$ NFs needs to be considered. A lot of heterojunctions are generated in rGO NS-loaded SnO$_2$ NFs. Because the loaded rGO NSs have a discrete configuration, main conduction will occur along continuous SnO$_2$ NFs, rather than along discrete rGO NSs. Since the work function of rGO is larger than that of SnO$_2$, at equilibrium, in order to align the Fermi level, electrons will flow from SnO$_2$ to rGO. Not only the developed barrier adds the additional modulation of total resistance of NFs by adsorption and desorption of H$_2$ molecules, but also the heterojunction will expand the depleted space in NFs. These potential barriers decrease or increase in height due to adsorption or desorption of hydrogen molecules, respectively, resulting in additional modulation of the resistance of NFs. The electron depletion layer is generated at the SnO$_2$ side of the heterojunctions. In case of reducing gas, the reducing gas reacts with the adsorbed oxygen (O$^-$) on the SnO$_2$ NF surface, subsequently providing electrons to the NFs.

13

Accordingly, the depletion region will be reduced. The sensors response of reducing gas to n-type semiconductor will be defined as $S = R_a/R_g$ (R_a: initial ambient resistance; R_g; resistance with the introduction of reducing gas). With the existence of a lot of SnO_2/rGO heterojunctions, the initial resistance (R_a) will be considerably increased. With the increased initial resistance, the modulation of resistance by the sensing target gas will turn out to be a higher sensitivity. Also, discrete rGO NSs on the surface will play a catalytic role, enhancing the adsorption, dissociation, and transport (to neighbouring SnO_2 surface) of H_2 gas.

2) Sensing mechanisms of rGO-loaded ZnO NFs (Same as Text S5)

Being similar to the rGO-loaded SnO_2 NFs, the rGO-loaded ZnO NFs will exhibit the resistance modulation, not only due to the change of the radial thickness of the electron-depletion layer, but also due to the change of the height of the potential barrier at nanograin boundaries. In Fig. 4 of the manuscript, it is depicted that a large amount of rGO NSs is descretly distributed in the ZnO NFs, without a direct contact between adjacent rGO NSs. In air ambient, in Fig. 4 of the manuscript, it is depicted that a large amount of rGO NSs is discretly distributed in the ZnO NFs, without a direct contact between adjacent rGO NSs. Since the work functions of n-ZnO and rGO were about 5.20 and 4.75 eV, respectively (Fig. 4 in the manuscript), the electrons will flow from metallic rGO to n-ZnO, ultimately equating the Fermi level of two components. Accordingly, at equilibrium, the potential barrier (~0.45 eV) will be formed when the rGO contacts the n-ZnO. It has been widely accepted that the presence of hydrogen on a ZnO surface noticeably enhances its electrical conductivity.[12,13] Surface hydrogen atoms are very shallow donors, forming strong bonds with surface O ions rather than incorporating into bulk ZnO.[14] These characteristics contribute to the surface metallization of ZnO. Among the several mechanisms regarding hydrogen-induced metallization[15-19], the ″reduction″ mechanism, also referred to as ″semiconductor to metallic transition″ or ″surface metallization effect,″ has been regarded as the most likely and explains the high sensitivity and selectivity to hydrogen in the case of pure

ZnO NFs at high temperatures.[21] Hydrogen-induced metallicity has been observed on a variety of surfaces, including ZnO (100),[13,18,20] ZnO (0001),[15] and ZnO ($2\bar{1}\bar{1}0$).[17] The delocalization of charge between Zn and O-H bonds induces metallization of surface Zn atoms.[21] The surface state of ZnO before and after H_2 exposure was investigated using XPS in our previous work,[21] confirming the transformation of the ZnO surface to metallic Zn. Since the introduction of H_2 gas inevitably generates metallic Zn layer along the rGO/ZnO heterojunctions, the energy band diagrams involving three phases should be considered (Fig. 4 in the manuscript). With the work functions of rGO, Zn, and ZnO being 4.75, 4.33, and 5.20 eV, respectively, at equilibrium, the potential barriers not only at the rGO/Zn interfaces but also at the Zn/ZnO interfaces will be generated. One possibility is that the n-ZnO will become more n-type, by the transfer of electrons from rGO. The above speculation is based on the assumption that the Zn metallic layer will not be generated. However, in reality, the metallic Zn layer will be provided upon the introduction of H_2 gas. In this case, n-ZnO will become much more n-type, by the transfer of electrons from metallic Zn. In this case, the adsorbed oxygen from ambient will more efficiently extract electrons from ZnO, enlarging the depletion region and thus decreasing the conduction region.[22,23] The hydrogen molecules will react with the adsorbed oxygen species. The released electrons will reduce the thickness of the depletion region, and decrease the resistance of the semiconductors. Upon introduction and removal of H_2 gas, the conduction region will be increased and decreased, respectively (i.e. depletion region will be decreased and increased, respectively). Since the original volume of the conduction layer in ZnO NFs is larger by the ZnO/rGO heterointerfaces, the relative change of the resistance by the H_2 gas will be larger, resulting in the higher sensitivity. The second possibility is associated with the electron flow of ZnO through the rGO NSs, ultimately providing additional modulation of resistance. With the neighboring NSs being disconnected, the electrical conduction will mainly occur through the ZnO NFs. In air ambient, the equilibrium energy band of ZnO is 0.45 eV higher than that of rGO, facilitating easy flow of electrons from ZnO to rGO. For the realization of electrical conduction through the rGO NSs, the electrons, which were penetrated from the ZnO into the rGO, should be taken out of the rGO NSs. In air ambient, however, the reverse flow from rGO to n-ZnO is not efficient and electrons in rGO cannot easily escape out to the neighboring ZnO grains, owing to the barrier height (i.e. 0.45 eV). On the other hand, in H_2 ambient, the potential barrier of

15

rGO/Zn will be established, preventing the electron flow into rGO. Accordingly, the electrons in sensor devices will be less lost to the rGO region. This will add to decrease of resistance by H_2 gas. As a third possibility, the rGO NSs will exert the spillover effect. The discretely distributed rGO NSs being attached to the surfaces of the NFs are nanostructures with a higher surface accessibility.[24] The NSs will exert a catalytic function in the adsorption, dissociation and migration of H_2 gas molecules. It is possible that the defects and functional groups on the rGO surface provide adsorption sites for the gas molecules and will increase the sensitivity.[22]

3) Comparison between the sensing mechanisms of rGO-loaded SnO$_2$ NFs and rGO-loaded ZnO NFs

	Mechanism 1	Mechanism 2	Mechanism 3	Mechanism 4
rGO-loaded SnO$_2$ NFs	SnO$_2$ NF surface depletion region	Potential barrier at SnO$_2$-SnO$_2$ homointerfaces	Potential barrier at SnO$_2$-rGO heterointerfaces	Spillover effect by rGO NSs
rGO-loaded ZnO NFs	ZnO NF surface depletion region	Potential barrier at ZnO-ZnO homointerfaces	Potential barrier at ZnO-rGO heterointerfaces + **Zn metallization**	Spillover effect by rGO NSs

Accordingly, rGO-loaded SnO$_2$ NFs and rGO-loaded ZnO NFs commonly exhibit the sensor mechanisms based on NF surface depletion region, potential barrier at semiconductor homointerfaces, and spillover effects by rGO NSs. However, in the mechanism with respect to the semiconductor/rGO interfaces, the rGO-loaded ZnO NFs additionally have a surface metallization effect of ZnO grain boundaries. We thereby surmise that the surface metallization effect of ZnO grain boundaries is a main factor for the superior sensor behavior of rGO-loaded ZnO NFs to rGO-loaded SnO$_2$ NFs .
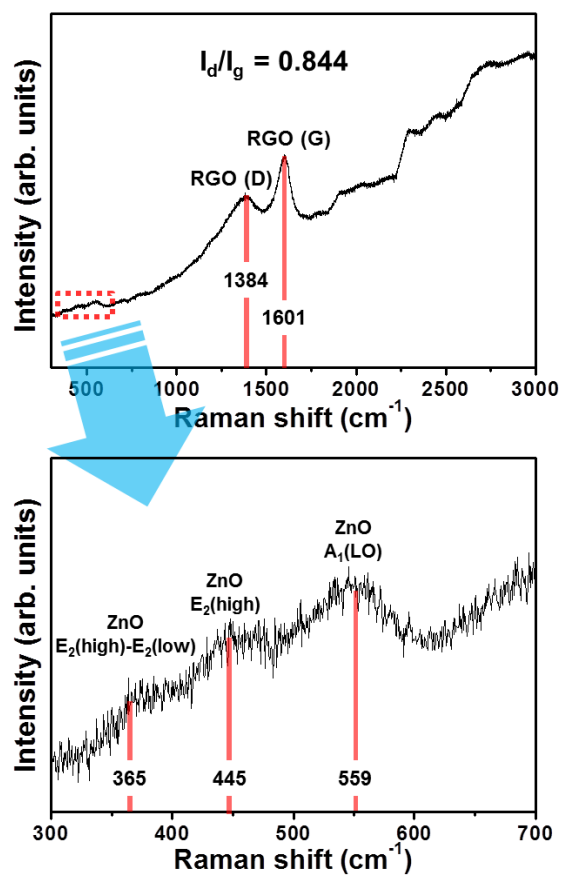
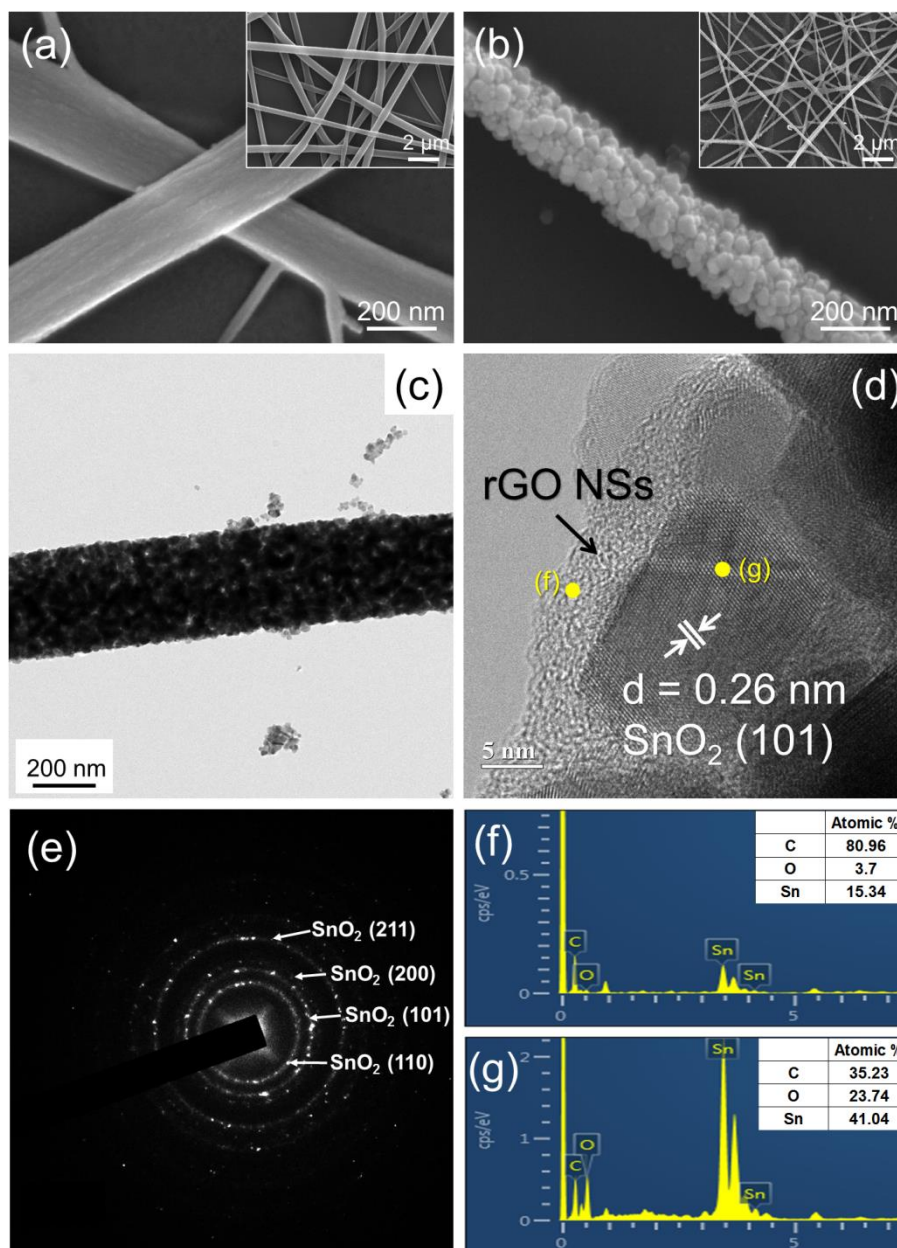**Fig. S1.** Raman spectrum of rGO-loaded ZnO NFs.

Fig. S2. SEM images of (a) as-spun and (b) calcined rGO-loaded SnO_2 NFs. (c) Low-magnification TEM image of a calcined rGO-loaded SnO_2 NFs. (d) TEM image of an enlarged surface region of (c). (e) Associated SAED pattern. (f,g) EDX spectra taken from the positions (f) and (g) in (d).
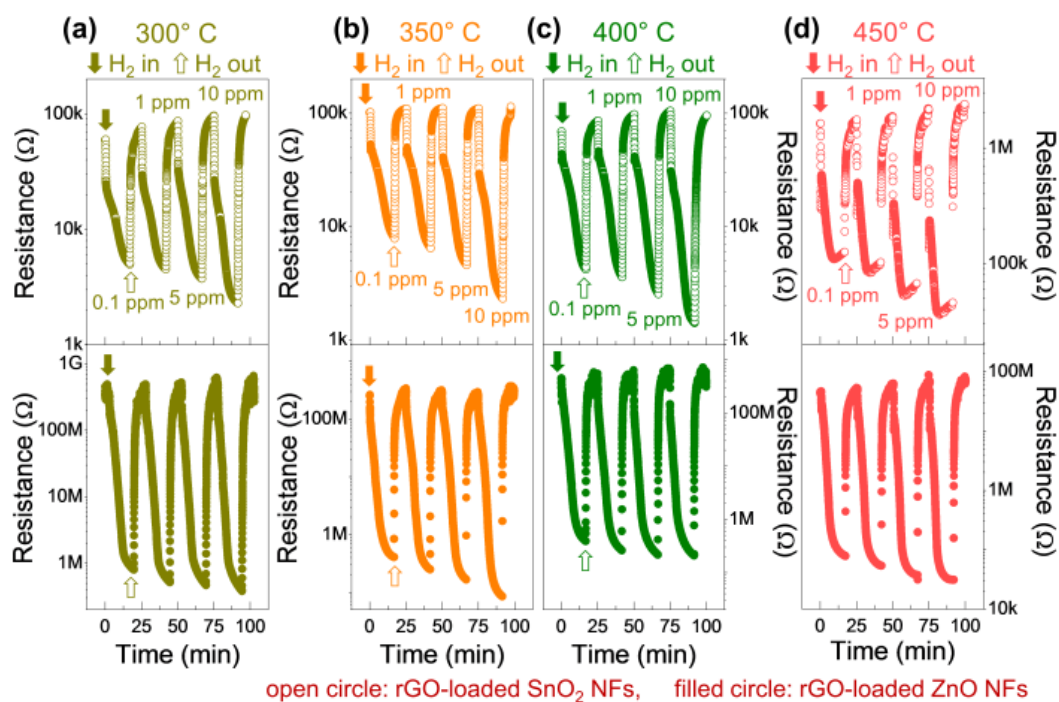
Fig. S3. Dynamic resistance curves of rGO/SnO$_2$ and rGO/ZnO composite NFs at (a) 300, (b) 350, (c) 400, and (d) 450°C (open circles: rGO-loaded SnO$_2$ composite NFs; filled circles: rGO-loaded ZnO NFs). The H$_2$ concentrations were set to 0.1, 1, 5, and 10 ppm, respectively.
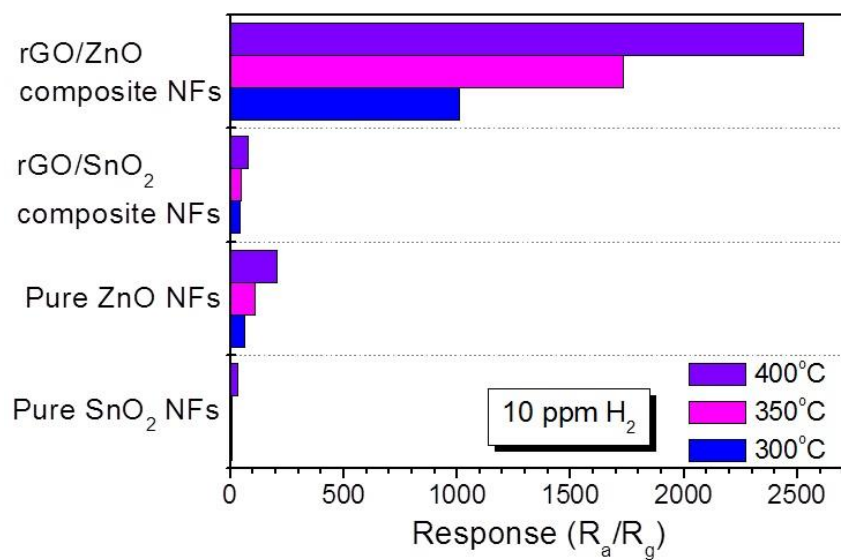
Fig. S4. Sensor responses of pure SnO$_2$ NFs, pure ZnO NFs, rGO-loaded SnO$_2$ NFs and rGO-loaded ZnO NFs at temperatures of 300-400°C and at the H$_2$ concentration of 10 ppm.
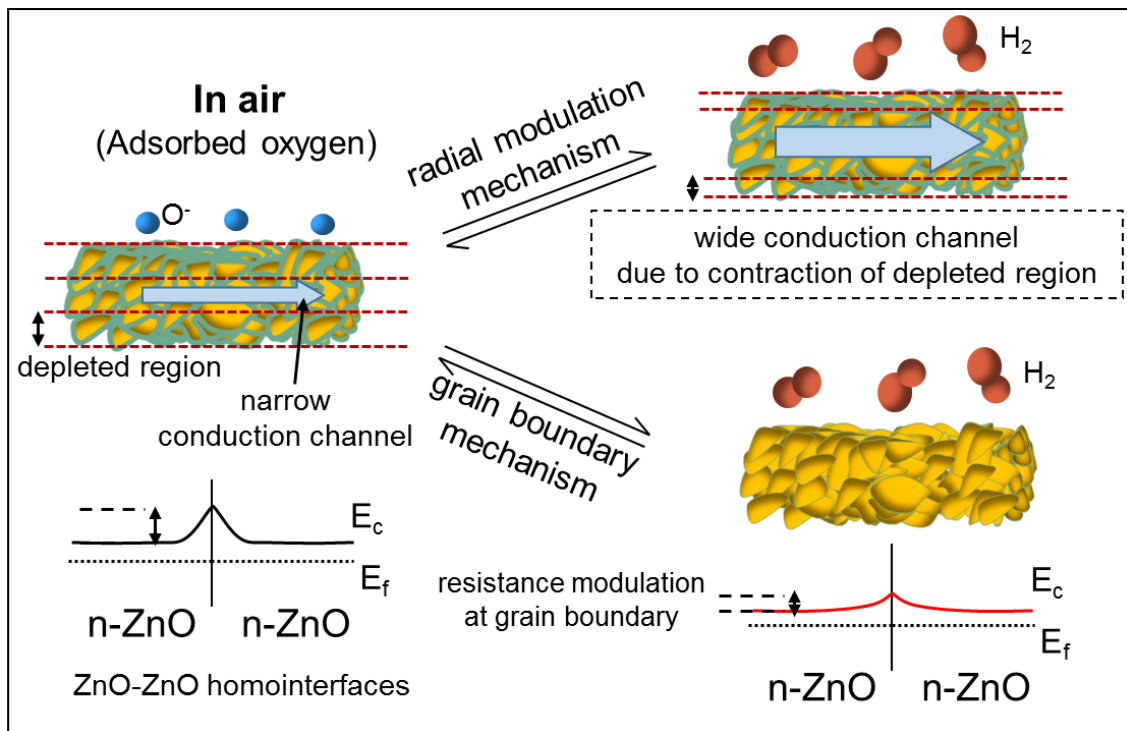
Fig. S5. Schematic diagram of sensing mechanisms in regard to pure ZnO NFs.

Table S1. Sensor responses of rGO-loaded SnO$_2$ NFs and rGO-loaded ZnO NFs at temperatures and H$_2$ concentrations in the range of 300-450 °C and 100ppb-10 ppm, respectively.

H$_2$ concentration	Response(R$_a$/R$_g$)							
	rGO/SnO$_2$ composite NFs				rGO/ZnO composite NFs			
	300°C	350°C	400°C	450°C	300°C	350°C	400°C	450°C
100 ppb	12.1	13.0	16.5	12.9	422.9	485.3	865.9	581.0
1 ppm	17.1	17.0	24.0	17.2	721.3	1019.3	1415.4	957.9
5 ppm	23.2	24.2	38.7	27.2	852.6	1593.2	2010.3	1657.4
10 ppm	42.0	47.8	74.8	41.8	1007.5	1731.6	2524.0	2028.0

Table S2. Sensor responses of rGO-loaded ZnO NFs at 400℃ to various gases.

	Response (R_a/R_g or R_g/R_a)		
	0.44 wt% rGO-loaded ZnO NFs		
	1 ppm	2 ppm	5 ppm
NO_2	91.5	110.0	119.0
SO_2	49.7	59.5	65.7
O_2	23.2	28.8	34.2
CO	7.7	9.7	22.6
C_6H_6	14.4	15.7	19.1
C_2H_5OH	14.9	15.8	19.1
H_2	1415.4	2010.3	2524.0

Table S3. Comparison of some recently developed highly sensitive and selective hydrogen sensors.

Material type	H$_2$ Concentration (ppm)	Temperature (ºC)	Response (R$_a$/R$_g$ or R$_g$/R$_a$)	Response time (90% change in the original resistance)	Recovery time (90% change in the original resistance)	Ref
Platinum-activated tungsten oxide (Pt-WO$_3$) films	200	200	8.5*	0.7 min	9 min	[25]
Pt/Nb$_2$O$_5$ nanowires	2000	RT	$\cong$ 98* %	1.67 min	7.83 min	[26]
Nanoporous TiO$_2$ thin films	50	500	50*	5-10 sec (50%)	$\leq$ 5 sec (50%)	[27]
Cadmium-doped ZnO nanowires (NWs)	100	RT	$\cong$ 280* %	14 sec (36.8%)	11 sec (36.8%)	[28]
ZnO nanorods	150	200	$\cong$ 3200* %	-	-	[29]
ZnO nanorods	1000	325	$\cong$ 200* %	-	-	[30]
Pd-decorated SnO$_2$ nanowires	10,000	RT	~1.2 x 10^{5*} %	~2 sec (36.8 %)		[31]
Aluminum doped porous TiO$_2$	1000	300	98.7* %	211 sec (63%)	-	[32]
Suspended, functionalized single tungsten nanowire	10,000	RT	11.52% increase in electrical resistance	19 sec	424 sec	[33]
Ultrasonically sprayed SnO$_2$ thin films	1000	350	3040	2 sec	12 sec	[34]
SnO$_2$ thin films	800	350	1142	-	-	[35]
ZnO nanowire	10	RT	0.020*	3 sec	2 sec	[36]
Undoped titania nanotubes	1000	RT	5 x 10^{10*} %	-	-	[37]
Polymer membrane-coated palladium NP/single layer graphene hybrid	2% in N$_2$	RT	66.37* %	1.81 min	5.52 min	[38]
Nanocomposite NiO:Au thin films	2000	167	~11	-	-	[39]
ZnO nanofibers	100 ppb (0.1 ppm)	300	63.8	-	-	[4]
Bi$_2$S$_3$ nanowires	10	RT	1.22	-	-	[40]
SnO$_2$ nanowires	10	300	< 0.5	-	-	[41]
rGO nanosheets loaded ZnO nanofibers	100 ppb (0.1 ppm)	400	866	3.5 min	3.9 min	This work

| rGO nanosheets loaded ZnO nanofibers | 10 | 300
400 | 1007.5
2524 | 3.4 min
0.9 min | 3.0 min
3.5 min | This work |

* $\Delta R/R$, where $\Delta R = R_g - R_a$ or $R_a - R_g$ and $R = R_a$

References

1 W. S. Hummers Jr and R. E. Offerman, *J. Am. Chem. Soc.*, 1958, **80**, 1339-1339.

2 J. H. Lee, A. Katoch, S. W. Choi, J. H. Kim, H. W. Kim and S. S. Kim, *ACS Appl. Mater. Inter.*, 2015, **7**, 3101-3109; Z. U. Abideen, A. Katoch, J.-H. Kim, Y. J. Kim, Y. J. Kwon, H. W. Kim, S. S. Kim, *Sensors and Actuators B: Chemical* (2015), http://dx.doi.org/10.1016/j.snb.2015.07.120.

3 Y. B. Zhang, J. Yin, L. Li, L. X. Zhang and L. J. Bie, *Sensor. Actuat. B-Chem.*, 2014, **202**, 500-507.

4 A. Katoch, S. W. Choi, H. W. Kim and S. S. Kim, *J. Hazard. Mater.*, 2015, **286**, 229-235.

5 K. A. Alim, V. A. Fonoberov, M. Shamsa and A. Balandin, *J. Appl. Phys.*, 2005, **97**, 124313.

6 Y. Wang, B. Meyer, X. Yin, M. Kunat, D. Langenberg, F. Traeger, A. Birkner and Ch. Wöll, *Phys. Rev. Lett.*, 2005, **95**, 266104.

7 X. L. Yin, A. Birkner, K. Hanel, T. Lober, Kohler and C. Woll, *Phys. Chem. Chem. Phys.*, 2006, **8**, 1477-1481.

8 A. B. Usseinov, E. A. Kotomin, A. T. Akilbekov, Y. F. Zhukovskii and J. Purans, *Phys. Scr.*, 2014, **89**, 045801.

9   I. Kuzmina and V. A. Nikitenko, *Zinc oxide, synthesis and optical properties*, Naouka, Moscow, 1984.

10 I. Barin, *Thermochemical Data of Pure Substances*, Weinheim, 2nd edn., 1995, vol.2

11 G. Bruno, M. M. Giangregorio, G. Malandrino, P. Capezzuto, I. L. Fragala and M. Losurdo, *Adv. Mater.*, 2009, **21**, 1700-1706.

12 H. Moormann, D. Kohl and G. Heiland, *Surf. Sci.*, 1980, **100**, 302-314.

13 Y. Wang, B. Meyer, X. Yin, M. Kunat, D. Langenberg, F. Traeger, A. Birkner and Ch. Wöll, *Phys. Rev. Lett.*, 2005, **95**, 266104.

14 A. B. Usseinov, E. A. Kotomin, A. T. Akilbekov, Y. F. Zhukovskii and J. Purans, *Phys. Scr.*, 2014, **89**, 045801.

15 K. Nishidate and M. Hasegawa, *Physical Review B*, 2012, **86**, 035412.

16 G. Heiland, E. Mollwo and F. Stöckmann, in *Solid State Phys.: Electronic processes in zinc oxide*, ed. S. Frederick and T. David, Academic Press, 1959, vol.8, 191-323.

17 C. Wang, G. Zhou, J. Li, B. Yan and W. Duan, *Physical Review B*, 2008, **77**, 245-303.

18 K. Ozawa and K. Mase, *Physical Review B*, 2010, **81**, 205322.

19 H. Xu, W. Fan, A. L. Rosa, R. Q. Zhang, T. Frauenheim, *Physical Review B*, 2009, **79**, 073402.

20 X. L. Yin, A. Birkner, K. Hanel, T. Lober, Kohler and C. Woll, *Phys. Chem. Chem. Phys.*, 2006, **8**, 1477-1481.

21 A. Katoch, S. W. Choi, H. W. Kim and S. S. Kim, *J. Hazard. Mater.*, 2015, **286**, 229-235.

22 K. Anand, O. Singh, M. P. Singh, J. Kaur, R. C. Singh, Sens. Actuators B 195 (2014) 409-415.

23 R. Zou, G. He, K. Xu, Q. Liu, Z. Zhang, J. Hu, J. Mater. Chem. A 1 (2013) 8445-8452.

24 Q. Lin, Y. Li, M. Yang, Sens. Actuators B 173 (2012) 139-147.

25 C. Zhang, A. Boudiba, C. Navio, C. Bittencourt, M. G. Olivier, R. Snyders and M. Debliquya, *Int. J. Hydrogen Energy*, 2011, **36**, 1107-1114.

26 Z. Wang, Y. M. Hu, W. Wang, X. Zhang, B. X. Wang, H. Y. Tian, Y. Wang, J. Guan and H. Gu, *Int. J. Hydrogen Energy*, 2012, **37**, 4526-4532.

27 C. Lu and Z. Chen, *Sensor. Actuat. B-Chem.*, 2009, **140**, 109-115.

28 O. Lupan, L. Chow, T. Pauporte, L. K. Ono, B. R. Cuenya, G. Chai, *Sensor. Actuat. B-Chem.*, 2012, **173**, 772-780.

29 J. J. Hassan, M. A. Mahdi, C. W. Chin, H. Abu-Hassan and Z. Hassan, *Sensor. Actuat. B-Chem.*, 2013, **176**, 360-367.

30 J. Huh, J. Park, G. T. Kim and J. Y. Park, *Nanotechnology*, 2011, **22**, 085502.

31 J. M. Lee, J. E. Park, S. Kim, S. Kim, E. Lee, S. J. Kim and W. Lee, *Int. J. Hydrogen Energy*, 2010, **35**, 12568-12573.

32 S. K. Hazra and S. Basu, *Sensor. Actuat. B-Chem.*, 2006, **115**, 403-411.

33 J. Choi and J. Kim, *Sensor. Actuat. B-Chem.*, 2009, **136**, 92-98.

34 L. A. Patil, M. D. Shinde, A. R. Bari and V. V. Deo, *Sensor. Actuat. B-Chem.*, 2009, **143**, 270-277.

35 N. S. Baik, G. Sakai, N. Miura and N. Yamazoe, *Sensor. Actuat. B-Chem.*, 2000, **63**, 74-79.

36 O. Lupan, V. V. Ursaki, G. Chai, L. Chow, G. A. Emelchenko, I. M. Tiginyanu, A. N. Gruzintsevf and A. N. Redkinf, *Sensor. Actuat. B-Chem.*, 2010, **144**, 56-66.

37 M. Paulose, O. K. Varghese, G. K. Mor, C. A. Grimes and K. G. Ong, *Nanotechnology*, 2006, **17**, 398-402.

38 J. Hong, S. Lee, J. Seo, S. Pyo, J. Kim and T. Lee, *ACS Appl. Mater. Inter.*, 2015, **7**, 3554-3561.

39 I. Fasaki, M. Kandyla, M. G. Tsoutsouva and M. Kompitsas, *Sensor. Actuat. B-Chem.*, 2013, **176**, 103-109.

40 K. Yao, W. W. Gong, Y. F. Hu, X. L. Liang, Q. Chen and L. M. Peng, *J. Phys. Chem. C*, 2008, **112**, 8721-8724.

41 B. Wang, L. F. Zhu, Y. H. Yang, N. S. Xu and G. W. Yang, *J. Phys. Chem. C*, 2008, **112**, 6643-6647.